Heliyon 9 (2023) e21979

Contents lists available at ScienceDirect

Heliyon

journal homepage: www.cell.com/heliyon

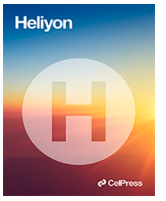

$ZnMn_2O_4$ nanostructures: Synthesis via two different chemical methods, characterization, and photocatalytic applications for the degradation of new dyes

Azam Sobhani [a,*], Samira Alinavaz [b]

[a] Department of Chemistry, Kosar University of Bojnord, Bojnord, 94531-55168, Iran
[b] Institute of Nano Science and Nano Technology, University of Kashan, Kashan, 87317-51167, Iran

ARTICLE INFO

Keywords:
Nanostructures
Co-precipitation
Hydrothermal
Photocatalyst
Zinc manganese oxide
Radical scavenger

ABSTRACT

Water pollution have become contentious among researchers. By increasing industrialization, the availability of clean water has been reduced. Industrial dyestuffs contribute to the escalation of environmental pollution and are the largest group of organic compounds. The aim of the present work is the synthesis of nanostructures that accelerate the removal of organic dyes from water. To reach this aim, first, $ZnMn_2O_4$ nanostructures were synthesized by hydrothermal and co-precipitation methods using maleic acid and phenylalanine as a capping agent. Second, the nanostructures were characterized. XRD analysis revealed the formation of $ZnMn_2O_4$ with diameters about 32.3 nm. SEM analysis showed the formation of the agglomerated spherical $ZnMn_2O_4$ nanostructures with diameters lower than 50 nm. EDX analysis confirmed the purity of the prepared samples with the presence of Zn, Mn, and O. FT-IR analysis confirmed the bonding between Mn and O at about 620 cm^{-1}. $ZnMn_2O_4$ nanostructures showed antiferromagnetic behaviors due to the super-exchange interactions between manganese ions. Finally, the photocatalytic behavior of the nanostructures was investigated for degradation of the anionic and cationic dyes. The results of the photocatalytic tests of two as-prepared samples via different methods were similar. The results exhibit a promising photocatalytic activity in the presence of 0.03 g photocatalyst for degradation of a dye solution with 10 ppm concentration. We introduced these conditions as optimum conditions and achieved maximum decolorization (92.43 %) in the 10 ppm of MV solution after 90 min. Also, we repeated six consecutive reaction cycles and observed a little activity loss after six reactions. We related this result to the high stability of the photocatalyst. We performed scavenging experiments to evaluate the active species involved in the photocatalytic process and plausible mechanisms. The photocatalytic degradation of MV decreased in the presence of TBA and BQ, respectively. This decrease indicated that OH° and $O_2^{\circ -}$ radicals are important active species in the MV degradation process.

1. Introduction

Environmental issues have become contentious among researchers, especially involving water pollution. All waste materials that cannot be broken down by water are named water pollution. Industrialization expansions make environmental pollution become

* Corresponding author.
E-mail address: sobhani@kub.ac.ir (A. Sobhani).

https://doi.org/10.1016/j.heliyon.2023.e21979
Received 19 July 2023; Received in revised form 27 October 2023; Accepted 1 November 2023
Available online 7 November 2023

worsen. Also, by increasing industrialization, the availability of clean water is reduced. Industrial dyestuffs contribute to the escalation of environmental pollution and are the largest group of organic compounds [1]. The dyes absorb wavelengths of light preferentially, thus appearing to be colored. The dyes and phenolic compounds are organic pollutants that cause environmental contamination, especially water pollution, and are also harmful to the human body. Every year, many synthetic dyes are generated. With the increasing demand for such dyeing compounds, pollution of water resources increases [2]. The food, chemical, and textile industries generate much local dye wastewater. The bulk of leftover dyes produced during the dyeing and finishing process are released into the environment and can reflect serious issues arising [3]. The source of the water pollution must be removed rapidly, so that additional water contamination does not occur. Natural and costly technological processes that cleanse the water need many times to remove the harmful substances from the water. There are some ways to remove pollution from aqueous solutions that depend on the source and the type of pollution, including chemical oxidation, ion exchange, membrane separation, electrochemical techniques, coagulation–-flocculation, adsorption and photocatalysis [4]. In this work, we use photocatalyst for the removal of dye pollutants from water. This way is considered as one of the important and efficient approaches to dismiss the dyes in wastewater [5–8].

Zinc manganite ($ZnMn_2O_4$) is a mixed metal oxide incorporated into the spinel structure. The spinel metal oxide nanostructures have the general chemical composition of AB_2O_4, in which A can be zinc, magnesium, manganese, iron, nickel, etc., B can be manganese, chromium, aluminum, iron, etc.; and O is oxygen. In this structure A is a bivalent ion at tetrahedral sites and B is a trivalent ion at octahedral sites [9]. Now a days, a great interest has been observed in spinel metal oxide nanostructures with AB_2O_4 formula due to their unique physical and chemical properties and applications [10–14]. Among these, Zinc manganite is interesting because of its high energy density, high theoretical capacity less toxicity to the environment, environmental friendliness, low oxidation potential, low material cost and low working potential [15–20]. $ZnMn_2O_4$ nanostructures (ZMO NSs) have applications in lithium rechargeable batteries, sensors, specific memory devices, thermistors, anode electrodes and photocatalysis [21–25]. Therefore, we have devoted our efforts to synthesizing this material. ZMO NSs nanostructures have been prepared using various methods. These methods have been summarized in Table 1.

In this work, first ZMO NSs are synthesized by two different methods, including hydrothermal and co-precipitation followed by heating at 500 °C. Then morphology, purity, properties, and applications of the products as-synthesized are compared. The hydrothermal is a one-step and suitable process for the synthesis of nanostructures with high purity, low aggregation and narrow crystallite size distribution [37]. The co-precipitation is a suitable process for commercial production because of simple preparation conditions, convenient technology, a short production cycle, and low requirements for equipment in this method. Preparing powders with large yields, small and uniform particle sizes, and uniform chemical composition are advantages of the co-precipitation method [38]. In the end, the as-prepared samples were tested as photocatalysts in the decomposition of dyes. Also, their photocatalytic performances were compared.

The hydrothermal, solvothermal, and precipitation methods have been used for the synthesis of zinc manganite nanostructures by

Table 1
Summary of the different methods and conditions used to synthesize ZMO NSs.

Reference	Application	Synthetic method	Fuel	Capping Agent	Precursors	Product
[26]	Anode in lithium-ion battery	Spray drying process aneeling at 400 °C and 1000 °C/3h	–	Citric acid	Mn/Zn nitrate salts	$ZnMn_2O_4$ nanopowders
[27]		Solvothermal 180 °C, 48h	–	Oleic acid	Mn/Zn acetate salts	$ZnMn_2O_4$ nanoparticles
[28]	–	Hydrothermal 170 °C/48h			Zn acetate/Mn nitrate/H_2O_2/ NaOH	$ZnMn_2O_4$ nanofibers, nanorods, nanowebs
[29]		Hydrothermal then calcination at 650 °C and 800 °C			α-MnO_2 nanorods	$ZnMn_2O_4$ nanorods
[19]	Anode in lithium-ion battery	Hydrothermal 160 °C for 18 h	–	Ethylen glycole	Mn/Zn acetate salts	$ZnMn_2O_4$/ZnO
[30]	Chemical nanosensor	Auto-combustion method then calcination	Urea/ glycine/L-alanine	–	Mn/Zn nitrate salts/KCl	$ZnMn_2O_4$ nanostructures
[31]	Photocatalyst for Congo red	Sol–gel	–	Tragacanth gum	Zn/Mn nitrate salts	$ZnMn_2O_4$ nanoparticles
[32]	Supercapacitor devices	Electrospinning then calcination at 400 °C/4 h	–	PVP	Mn/Zn acetate salts	ZnMn2O4 nanofibers
[33]	Anode in lithium-ion battery	Ultrasonic spray pyrolysis then annealing at 500 °C/2h	–	–	Mn/Zn nitrate salts	Hierarchical porous $ZnMn_2O_4$
[34]	Electrochemical performance	Hydrothermal 100 °C/4h	–	–	Mn/Zn acetate salts	$ZnMn_2O_4$
[35]	Anode in rechargeable lithium-ion battery	Hydrothermal then calcination at 180 °C/24h	–	Nitrilotriacetic acid	Mn/Zn chloride salts	$ZnMn_2O_4$ nanowires
[36]	Anode in rechargeable lithium-ion battery	Solvothermal with ethylene glycol then calcination at 600 °C/2h	–	–	Mn/Zn nitrate salts	Pomegranate-shaped $ZnMn_2O_4$
		Hydrothermal then calcination at 600 °C/2h	–	–	Mn/Zn nitrate salts	$ZnMn_2O_4$ microspheres

some researchers. In the former articles, $ZnMn_2O_4$ nanostructures have been synthesized via hydrothermal plus calcination processes [12,39]. N. Guo was used from metal chlorides in the presence of EG via hydrothermal synthesis at 200 °C for 24 h plus calcination at 600 °C. Guo synthesized $ZnMn_2O_4$ microspheres [12]. Azmoodeh was used from metal nitrates in the presence of urea and ascorbic acid to synthesize the $ZnMn_2O_4$ microspheres. She used a hydrothermal (160 °C) plus calcination (500 °C) process for this synthesis [39]. M. Annalakshmi synthesized $ZnMn_2O_4$ using urea and ethylene glycol from nitrate salts via a solvothermal method at 180 °C plus a calcination process [40]. In the present work, we synthesize the pure $ZnMn_2O_4$ nanostructures via hydrothermal without calcination process. Therefore, the current method is simple and almost fast. The hydrothermal temperature used in this work (120 °C) is lower compared to previous works. The low hydrothermal temperature is an advantage for this research. The precursors used in this research are different than other works. F. Zhu prepared $ZnMn_2O_4$ from metal sulfates at 180 °C via a hydrothermal route. Then photocatalytic behavior of the manganites in the presence of organic acids was studied [41]. The precipitation plus calcination processes were also used to synthesize zinc manganites from manganese carbonate and zinc nitrate by N.M. Deraz in a high calcination temperature (800 °C). In the present co-precipitation process, a 500 °C calcination temperature has been selected [42].

Most researchers have studied the catalytic behavior of zinc manganite composites, for example, $ZnMn_2O_4$/ZnO [43], $ZnMn_2O_4$/ZnS/ZnO/PVP [44], $ZnMn_2O_4$/MnO_2 [45], $ZnMn_2O_4$/Mg [46], $ZnMn_2O_4$/TiO_2 [47] composites. In this work, we study the photocatalytic behavior of $ZnMn_2O_4$ nanostructures for the methyl violet (MV), erythrosine (ES), and eriochrome Black T (EBT) degradations, for the first time. A high degradation percent and good performance rate was achieved and reported for MV and these nanostructures in this study.

2. Experimental

2.1. Materials and experiments

All the materials, including $Zn(NO_3)_2.6H_2O$, $Mn(NO_3)_2.4H_2O$, and NH_3 (25 %), were in analytic grade, prepared by Merck company, and used without further purification. A Philips X'pertPro diffractometer with $\lambda = 1.54$ Å and Ni-filtered Cu Kα radiation was used to study XRD patterns. This diffractometer was made by Holland company. The anode, voltage, current, and scanning rate used in this apparatus were Cu, 40 kV, 30 mA, and 0.05°/s, respectively. A TESCAN Mira3 FE-SEM was used to study morphology and investigate the EDS spectrum. The sample was scanned with an electron beam (accelerated at 10 kV) to produce magnified SEM images. High-resolution images of the products were recorded at magnifications from 2kx to 100kx. The EDS component of the system was applied in conjunction with SEM analysis to determine elements for qualitative information. We take TEM images on a Philips EM208 transmission electron with 200 kV voltage. To be imaged using TEM, the sample has to be very thin and placed inside a high vacuum. Sample preparation is a crucial step in TEM, depending on the nature of the material. A Nicolet IS 10 spectrophotometer, made by the American Thermo Scientific Company, was used to study the FT-IR spectrum. We mixed some powder and KBr. Then, we ground them in a mortar and placed them in a press at 5000–10000 psi to form a disc. The disc was placed in the apparatus to take the FT-IR spectrum. An Evolution 300 spectrophotometer made by the American Thermo Scientific Company was used to study UV–Vis spectra. We dissolved the samples in a suitable solvent before analysis. A Meghnetic Kavir Kashan Co. VSM made in Kashan was used to study the magnetization. We equipped the apparatus with a 5 kW magnet power and used a frequency of ranging from 25 to 80 Hz. The magnet could supply a 2.5 T maximum field.

2.2. Hydrothermal synthesis of $ZnMn_2O_4$ nanostructures

An aqueous solution containing 0.368 g of $Zn(NO_3)_2.6H_2O$ was prepared. Then surfactant was added into it. Maleic acid and phenylalanine were used as surfactants in this synthesis. After stirring for 60 min, an aqueous solution containing 0.623 g of $Mn(NO_3)_2.4H_2O$ was added drop-wise into the solution under stirring. The stoichiometric ratio of Mn:Zn:surfactant was 2:1:6.5. Then NH_3 was added as a pH regulator. The solution was adjusted to pH = 9. The final solution was transferred into a stainless steel Teflon-lined autoclave and maintained at 120 °C for 12 h. The autoclave was cooled to room temperature on its own with the rate of 1 °C/min. The nanostructures were centrifuged and washed with distilled water and anhydrous ethanol several times.

2.3. Co-precipitation synthesis of $ZnMn_2O_4$ nanostructures

An aqueous solution containing 0.368 g of $Zn(NO_3)_2.6H_2O$ was prepared. Then phenylalanine, aqueous solution of $Mn(NO_3)_2.4H_2O$ (0.623 g) and NH_3 were added into the solution under stirring, respectively. The stoichiometric ratio of Zn:Mn:surfactant was 1:2:6.5. After stirring for 60 min, the product was centrifuged and washed with distilled water and anhydrous ethanol several times. In the next stage, in order to remove impurities, the products were heated at 500 °C for 2h under vacuum. The synthetic conditions investigated in

Table 2
The reaction conditions of ZMO NSs synthesized in this work.

Surfactant	Time (h)	Temperature (°C)	Mn source	Zn source	Synthesis method	Sample
maleic acid	12	120	$Mn(NO_3)_2.4H_2O$	$Zn(NO_3)_2.6H_2O$	hydrothermal	1 (54)
phenylalanine	12	120	$Mn(NO_3)_2.4H_2O$	$Zn(NO_3)_2.6H_2O$	hydrothermal	2 (51)
phenylalanine	2	500	$Mn(NO_3)_2.4H_2O$	$Zn(NO_3)_2.6H_2O$	co-precipitation	3 (52)

this work have been summarized in Table 2.

2.4. Photocatalytic measurements

Three dyes, MV, ES, and EBT, were used as contaminants to investigate the photocatalytic property of ZMO NSs. 30 mg ZMO photocatalyst were weighted and used to accelerate the dye degradation reaction. In this study, concentration and volume of dye solutions used were 10 ppm and 30 mL, respectively. The photocatalytic experiments were studied in a quartz reactor and under visible irradiation. The suspension, containing dye and photocatalyst, was aerated in darkness, stirred for 15 min, and placed at a space of 40 cm away from the visible lamp. After 10 min visible irradiation, the suspension was sampled, and centrifuged to remove the remained photocatalysts of the dye solution. Then, the absorbance spectrum of the solution was recorded, and photodegradation efficiency using the below equation was estimated. A_0 and A are absorbance quantities of dye solution before and after degradation, respectively [48].

$$\text{Degradation } \% = [(A_0\text{-}A) / A_0] \times 100 \quad (1)$$

In this study, three effects including dye type and concentration, and also photocatalyst dose on the photocatalytic performance of ZMO NSs were investigated. For recyclability tests, the photocatalyst was regenerated, washed with distilled water, dried at 70 °C, then reused. The scavenging experiments were similar to the photodegradation experiments. Two scavengers were selected, *tert*-butyl alcohol (TBA) and 1,4-Benzoquinone (BQ). Scheme 1 shows a schematic diagram of the synthesis of ZMO NSs and their photocatalytic applications.

2.5. XRD results

Fig. 1 shows XRD patterns of the products prepared from Zn and Mn salts via hydrothermal method at 120 °C for 12h. XRD technique is used to determine the crystallographic structure of materials. The product prepared in the presence of maleic acid (sample 1) is pure $ZnMn_2O_4$ (Fig. 1a). Broad peaks of XRD in Fig. 1a indicate small particle sizes in the product. The diffraction peaks in this figure match those of standard tetragonal spinel phase $ZnMn_2O_4$ (JCPDS No. 01–077–0470). These peaks at 2theta values of 18.23, 29.51, 31.29, 33.30, 36.47, 39.08, 44.81, 52.11, 54.47, 59.08, 60.96, and 65.19 correspond to crystal planes of (101), (112), (200), (103), (211), (004), (220), (105), (312), (321), (224) and (400). The XRD pattern of sample 2, prepared in the presence of phenylalanine in Fig. 1b shows two peaks at 2theta about 11 and 16.7, which failed to be identified from among the JCPDS cards. Other peaks with low intensity in this figure belong to $ZnMn_2O_4$ with JCPDS No. 01–077–0470. Thus, we selected maleic acid as the optimum

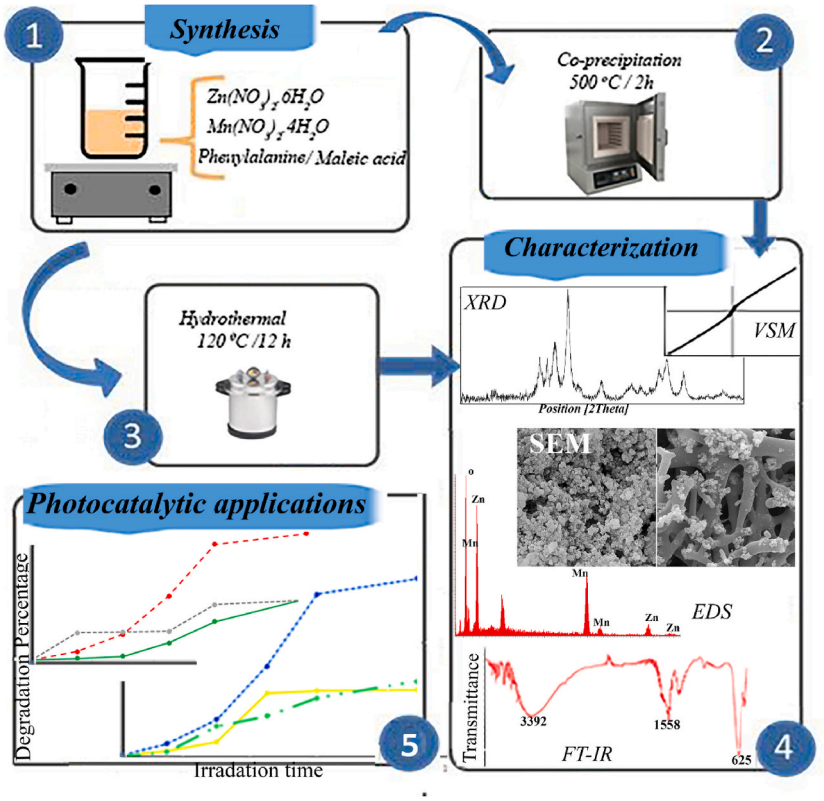

Scheme 1. Schematic diagram of the preparation and investigation of the photocatalytic activity of ZMO NSs.

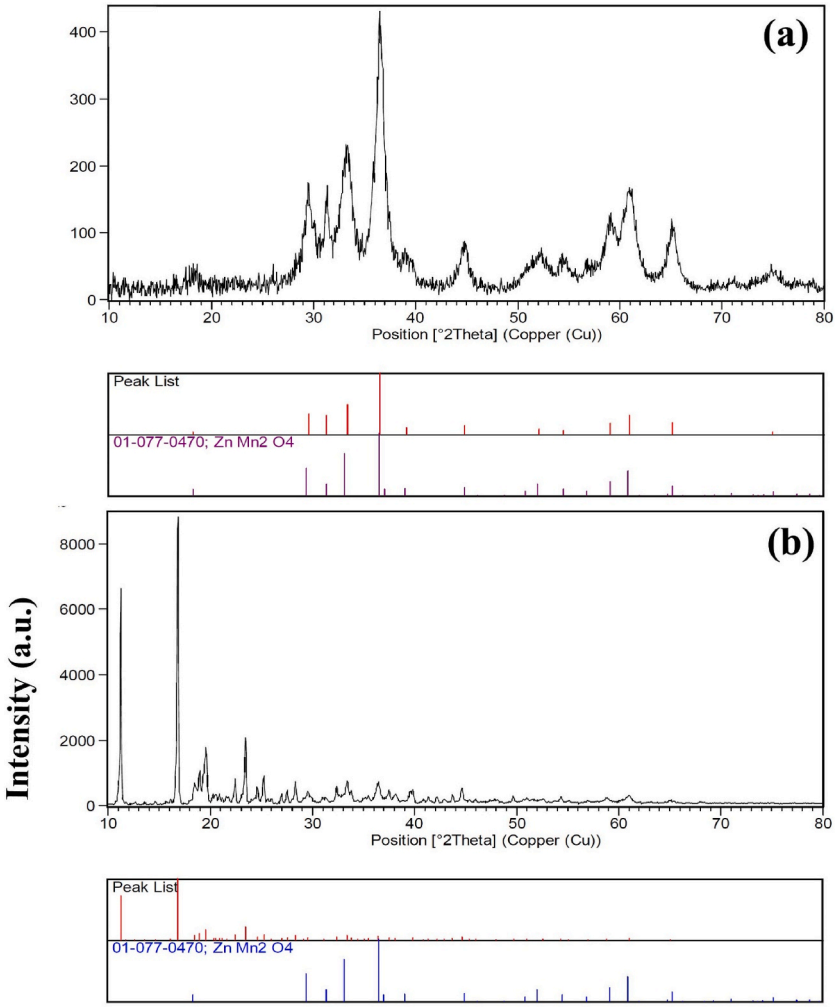

Fig. 1. XRD patterns of the products prepared from Zn and Mn salts via hydrothermal method at 120 °C for 12h, in the presence of different surfactants: (a) maleic acid (sample 1) and (b) phenylalanine (sample 2).

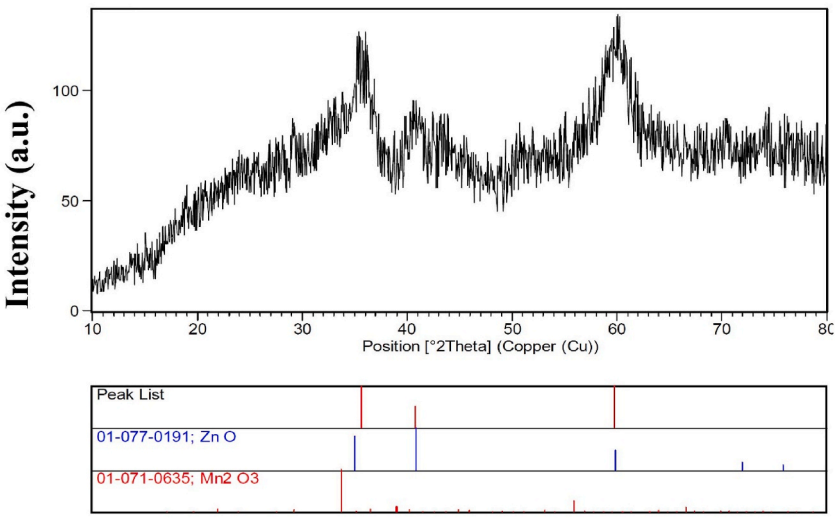

Fig. 2. XRD pattern of the product prepared from Zn and Mn salts in the presence of phenylalanine via co-precipitation method (sample 3).

surfactant for the hydrothermal synthesis of $ZnMn_2O_4$. Maleic acid is a dicarboxylic acid, and phenylalanine is an essential α-amino acid. Both have been selected as surfactants in this study.

XRD pattern of sample 3 prepared via the co-precipitation method shows the formation of ZnO and a small amount of Mn_2O_3, as shown in Fig. 2. Broad peaks of XRD indicate small particle sizes in the product. Also, low-intensity peaks indicate the low crystallinity of the product. By comparing XRD results in Figs. 1 and 2, we selected the hydrothermal method as the optimum method in the present work conditions. The average particle size of sample 1 was calculated 32.3 nm, by Scherrer equation, by using the X-ray line broadening analysis of the main diffraction line of this sample [17].

$$D = \frac{K\lambda}{\beta \cos\theta} \tag{2}$$

where, D is the average crystallite size, K is dimensionless shape factor (Scherrer constant, 0.89), λ is the X-ray wavelength, β is the full width at half maximum (FWHM) of ZMO NSs diffraction lines and θ is Bragg angle (diffraction angle of the phases under investigation).

2.6. SEM and EDS results

SEM images of the ZMO nanostructures prepared via two different methods have been shown in Fig. 3. Fig. 3 shows the formation of the agglomerated spherical ZMO nanoparticles in both samples 1 and 3 prepared via hydrothermal and co-precipitation methods. As shown in Fig. 3a–c, the diameters of the nanoparticles in sample 1 are lower than 50 nm. In SEM images of sample 3, nanorods are also seen in addition to these nanoparticles. SEM images with lower magnifications of this sample in Fig. 3d, e and f show that the nanorods connected and formed pseudo sponge or porous structures.

EDS is an analytical method for chemical characterization of materials. It shows the peaks correlated to the elemental composition of the sample. EDS is based on the emission of a specimen characteristic X-rays. A beam of high energy charged particles is focused into the investigated sample. An electron from a higher binding energy electron level falls into the core hole and an X-ray with the energy of the difference of the electron level binding energies is emitted. EDS spectrum of ZMO NSs prepared via both hydrothermal and co-precipitation methods (samples 1 and 3) have been shown in Fig. 4a and b, respectively. The figure shows the presence of Mn, O and Zn elements in both samples and confirms XRD results. EDS results have been summarized in Table 3.

2.7. FT-IR results

IR radiation can stimulate the movement of molecules and atomic bonds when it is directed at a matter. This movement takes different forms, for example, vibration or rotation. Depending on how the molecule is excited, information about the structure and identity of the irradiated material can be obtained. The adsorption of the IR radiation by a material is the basic requirement for its analysis with this spectrum. IR relies on the fact that most molecules absorb infrared light and convert it to molecular vibration. The adsorption of infrared light is because of the nature of the chemical bonds in a sample. FT-IR shows this absorption as a function of wavelength. FT-IR spectra of both samples prepared via co-precipitation and hydrothermal methods (samples 3 and 1) have been

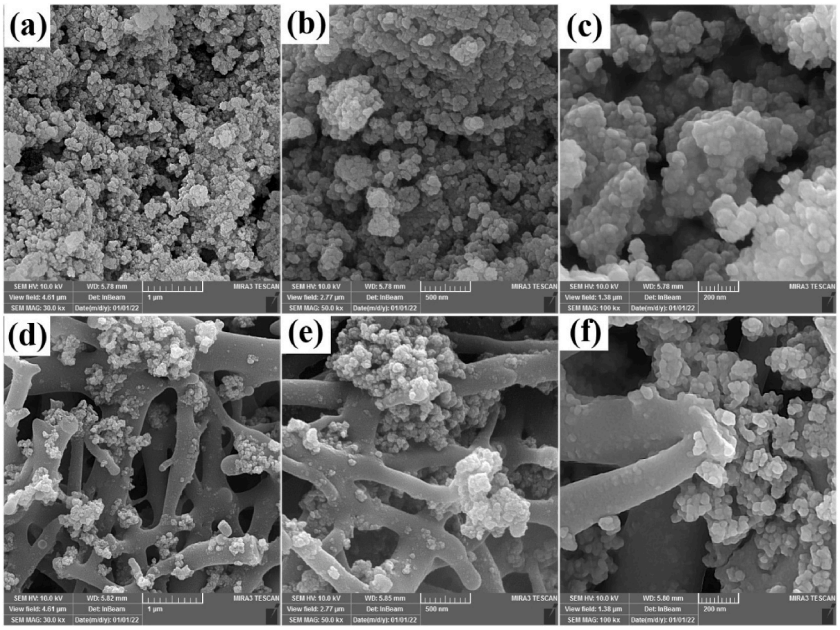

Fig. 3. SEM images of the ZMO NSs prepared via: (a–c) hydrothermal method (sample 1), (*d*–f) co-precipitation method (sample 3).

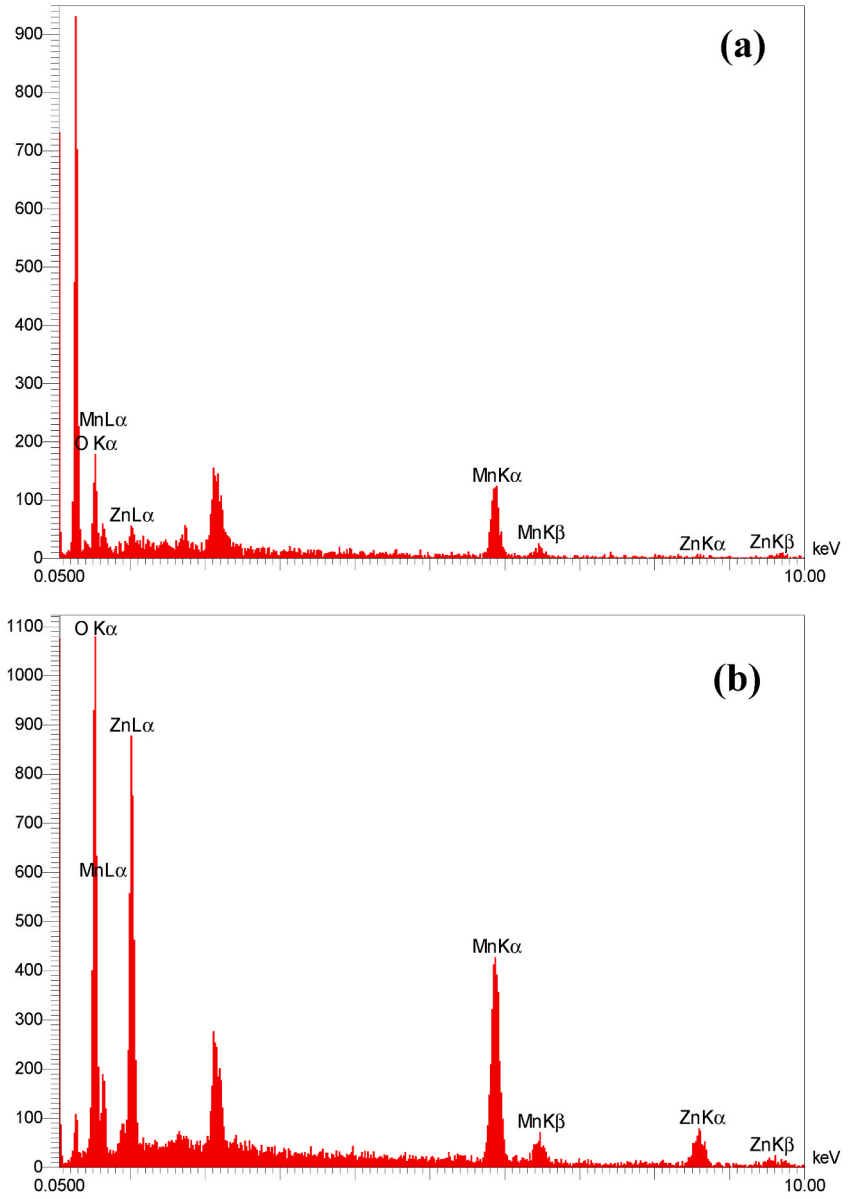

Fig. 4. EDS spectra of the ZMO NSs prepared via: (a) hydrothermal method (sample 1) and (b) co-precipitation method (sample 3).

Table 3
EDS results of ZMO NSs prepared via hydrothermal and co-precipitation methods.

A%	W%	Intensity	Line	Element	Sample
61.73	31.67	14.7	Ka	**O**	
35.50	62.54	24.4	Ka	**Mn**	Sample 1
2.77	5.80	0.6	Ka	**Zn**	
100.00	100.00				
67.09	35.69	94.3	Ka	**O**	
20.87	38.13	96.4	Ka	**Mn**	Sample 3
12.04	26.17	18.8	Ka	**Zn**	
100.00	100.00				

shown in Fig. 5a and b, respectively. The peaks in this figure are attributed to O–H, H_2O, C–OH and Mn–O vibrations, as summarized in Table 4. FT-IR results in Fig. 5 confirm formation of $ZnMn_2O_4$ nanostructures.

2.8. TEM results

Fig. 6a–c shows TEM images of the ZMO NSs prepared via hydrothermal method, duo to further investigation of morphology of sample 1. The images confirm formation of the nanospheres with diameters less than 50 nm.

3. UV–vis results

The photocatalytic activity of a photocatalyst, as a key factor determining the photocatalytic performance, is related to its light absorption capacity. The UV–Vis spectra were used to study the light absorption performance of samples 1 and 3. The results have been shown in Fig. 6d and e. Both samples show a broad peak in the wavelength range of 200–500 nm in UV–Vis spectra. Insets of Fig. 6d and e shows plots of $(\alpha h\nu)^2$ against hv. α is the absorption coefficient, and hν is the energy band gap. As shown in the insets, we calculated the optical band gaps (E_g) of samples 1 and 3 by the Tauc plot method to be about 2.2 eV and 2.3 eV, respectively.

3.1. Magnetic properties

VSM is a versatile technique for measuring the magnetic moment of samples. This technique gives this moment as a function of the applied magnetic field. Fig. 7a and b shows the magnetization curves of samples 1 and 3 measured using VSM. The figure shows antiferromagnetic behaviors for both samples prepared via hydrothermal and co-precipitation methods. It is due to the contribution of super-exchange interactions between Mn^{3+} and Mn^{4+} ions. Also, ferromagnetic behaviors observe in low fields in this figure.

3.2. Photocatalytic properties

The as-prepared ZMO NSs show photocatalytic activity. The photocatalyst degradation of three dyes was studied in the presence of sample 3. The results have summarized in Fig. 8. The photocatalytic degradation of dyes is influenced by several parameters. In this work, effects of type and concentration of dyes, and also photocatalyst dose are studied for the degradation of dyes. Fig. 8a shows that sample 3 is not a suitable photocatalysts for MV and ES degradation. But the EBT degradation percent is reported about 61 % after 60 min visible irradiation, in the presence of sample 3. Thus, EBT was selected as optimum dye and effects of dye concentration and photocatalyst dose were investigated for the degradation of this dye. Increasing photocatalyst dose led to raising the quantity of

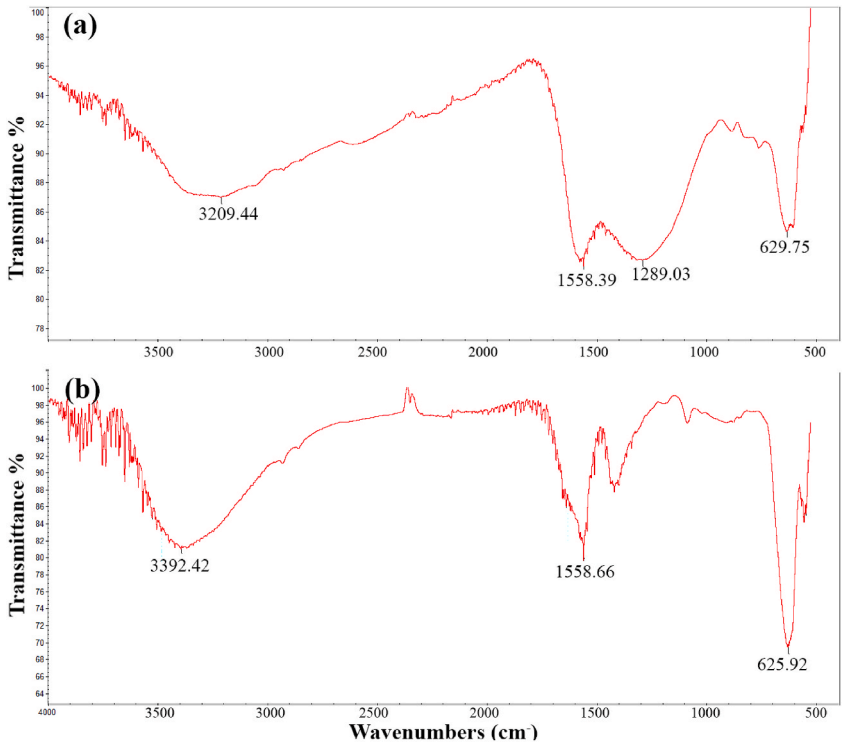

Fig. 5. FT-IR spectra of the ZMO NSs prepared via: (a) co-precipitation method (sample 3) and (b) hydrothermal method (sample 1).

Table 4
The assignment of FT-IR bands of the products.

Mn–O vibrations	C–OH vibrations of residual organic groups	H_2O bending vibrations	O–H stretching vibrations	Fig.	Synthesis method	Sample
629.75	1289.03	1558.39	3209.44	Fig. 4a	Co-precipitation	3
625.92	~1420	1558.66	3392.42	Fig. 4b	Hydrothermal	1

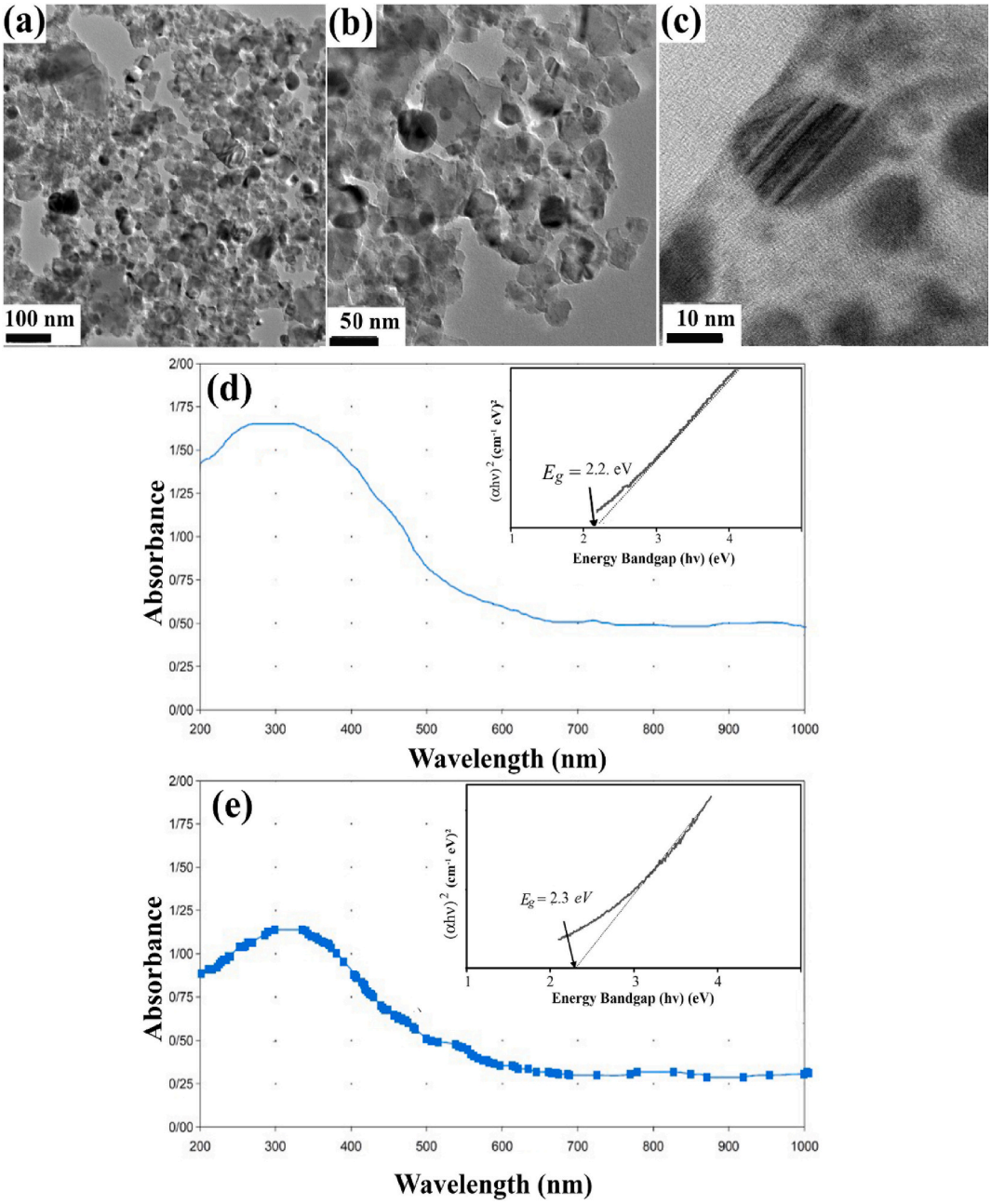

Fig. 6. (a–c) TEM images of the ZMO NSs prepared via hydrothermal method (sample 1), (d, e) UV–Vis diffuse reflectance spectra of samples 1 and 3, respectively. Insets of Fig. 6d and e shows the plots of $(\alpha h\nu)^2$ versus $h\nu$.

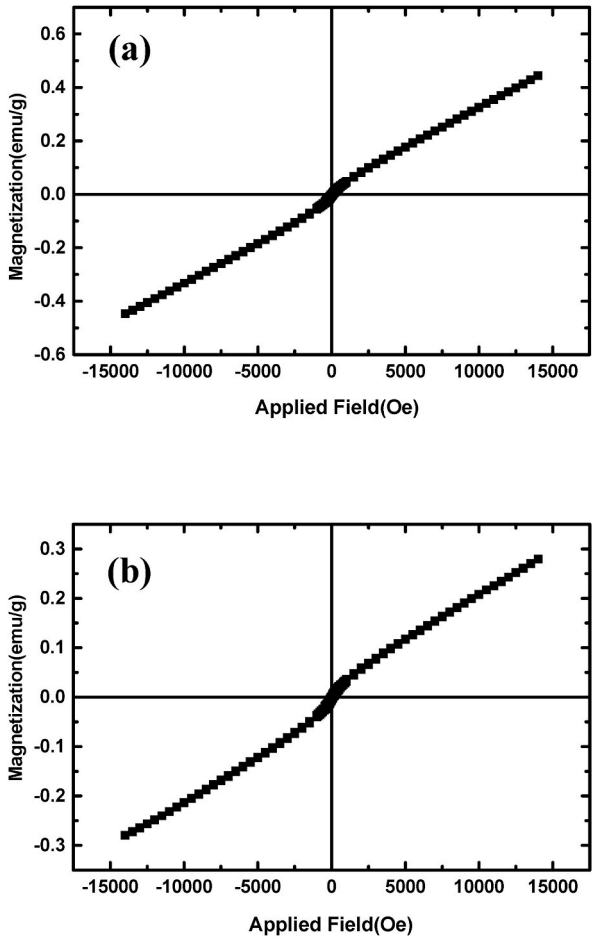

Fig. 7. Hysteresis curves of the ZMO NSs prepared via: (a) hydrothermal method (sample 1) and (b) co-precipitation method (sample 3).

adsorbed EBT and increasing the quantity of the photogenerated oxidizing radicals. Thus, increasing photocatalyst dose led to increasing EBT degradation percentage, as shown in Fig. 8b. Utilizing greater quantities of the photocatalyst (0.05g), EBT degradation percentage decreases. This decrease can be attributed to two reasons: (1) unsaturation of adsorption sites and (2) aggregation resulting from high photocatalyst dose. Fig. 8b shows 61 % degradation percentage in the presence of 0.03 g photocatalyst (sample 3) after 60 min. Effect of dye concentration was also investigated in this research. Fig. 8c shows the EBT degradation increases with increasing its concentration from 5 ppm to 10 ppm and then declines for EBT solution with 15 ppm concentration. The increase in the degradation percentage after increasing the EBT concentration is an interesting result. This result increases importance of the synthesized nanostructures in this work and their application for EBT degradation. Decreasing degradation percentage with enhancing dye concentration may be due to these agents: 1) lowering of light penetrating power, 2) lowering the production of electron and hole pairs, 3) lowering the rate of photodegradation, 4) Increasing competition between dye molecules and generated oxidizing agents to be adsorbed on the ZMO surfaces, 5) Reducing number of available oxidant molecules. Thus, the time required for the decolorization of dye solution is found to depend significantly on the initial dye concentration. The EBT degradation percentages were reported 25.15 %, 60.64 % and 14.18 % for 5, 10 and 15 ppm solutions, after 60 min, respectively.

In continuation, the photocatalytic degradation of ES and MV were investigated in the presence of sample 1, as shown in Fig. 9a. The experiments have been conducted in the presence of 0.03 g photocatalyst (sample 1) and 10 ppm dye solution. The degradation percentages of ES and MV after 90 min of visible light irradiation were about 57 % and 92 %, respectively. Thus, MV was selected as optimized dye and the effects of the photocatalyst dose and dye concentration were studied for its degradation in the presence of sample 1. Fig. 9b shows the effect of the dye concentration on the degradation of MV in the presence of 0.03 g sample 1. It is clear from this figure that the degradation rate of MV increases with decreasing its concentration from 15 ppm to 10 ppm and then declined for solution with 5 ppm concentration. With increasing MV concentration from 10 ppm to 15 ppm, degradation percentage is decreased from about 92 % to 45 % within 90 min of irradiation. Also, the effect of the photocatalyst dose in photocatalytic activity of sample 1 for degradation of a solution of MV with 10 ppm concentration was investigated (Fig. 9c). In contrast with dye concentration, photocatalyst dose exhibits an opposite behavior, registering a positive effect on ZMO degradation. The dye removal efficiency improves with the increase in the photocatalyst dose. This is mainly due to increase in the generated oxidizing agents and also increase in the

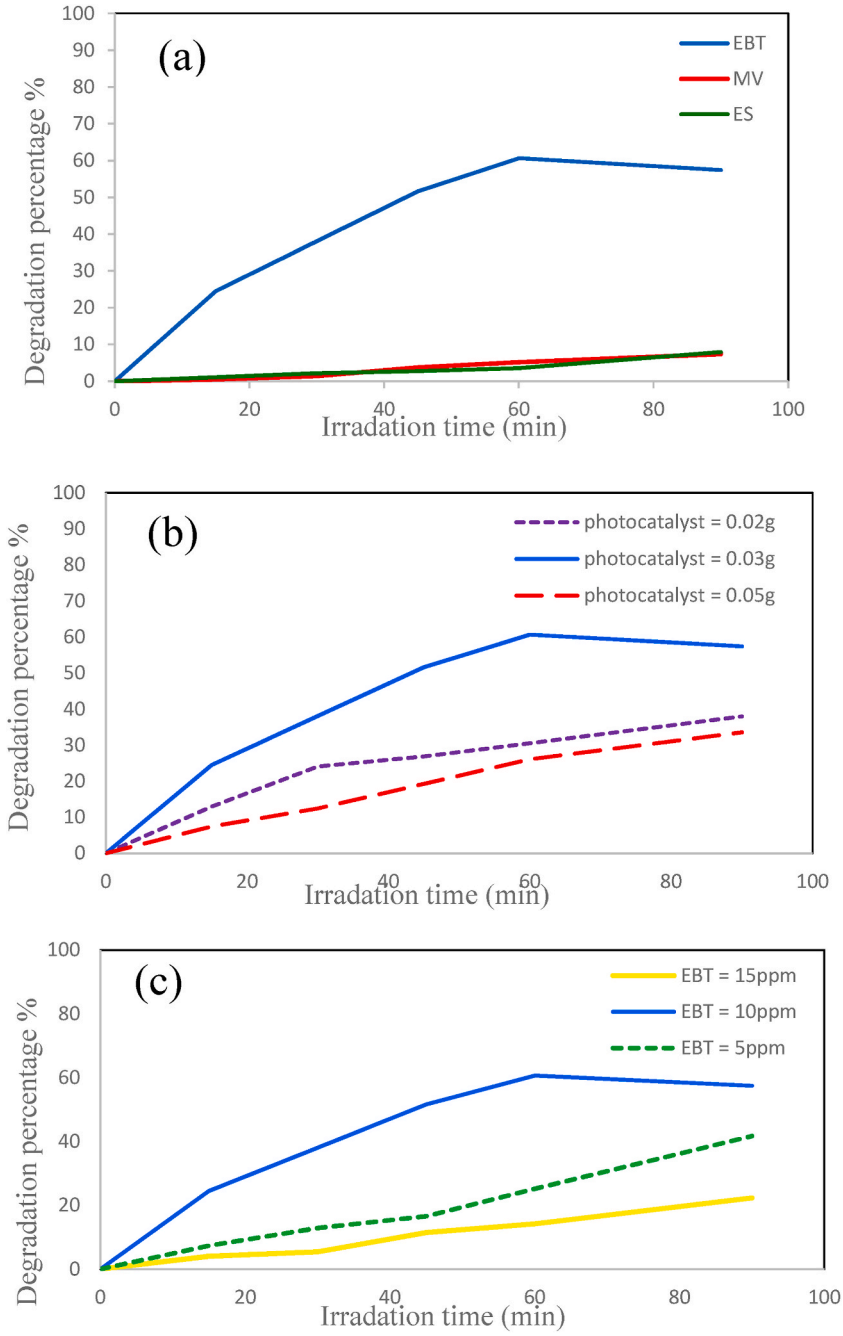

Fig. 8. The photocatalytic performance of sample 3 under visible light irradiation and investigation of the effects of: (a) dye type, (b) photocatalyst dose and (c) dye concentration.

number of free radicals (°OH and $O_2^{\circ-}$) in solution and active sites on the ZMO surfacs, which result in greater dye degradation. It is observed that removal efficiency of MV increases with increase in catalyst dose up to 0.03 g (optimum dose). Further increase in catalyst dose results in a decrease in the dye removal efficiency. This can be due to the aggregation of the suspended ZMO particles together in the high photocatalyst doses. This aggregation reduces the amount of sunlight reaching the active sites of the photocatalyst and thus the rate of photocatalyst reaction decreases [49,50]. Fig. 9c shows the higher photocatalytic performances of ~92 % for 0.03 g CMO after 90 min of irradiation, while only 38 % and 34 % degradation percentage of MV is observed for 0.02 g and 0.05 g CMO, respectively. The results indicate that 0.03 g ZMO-based photocatalyst is superior to that of others. The results of the photocatalyst tests for samples 3 and 1 have been summarized in Table 5.

Also, we included the control of MV, ES and EBT without catalysis to see whether the light exhibits some degradation. The results

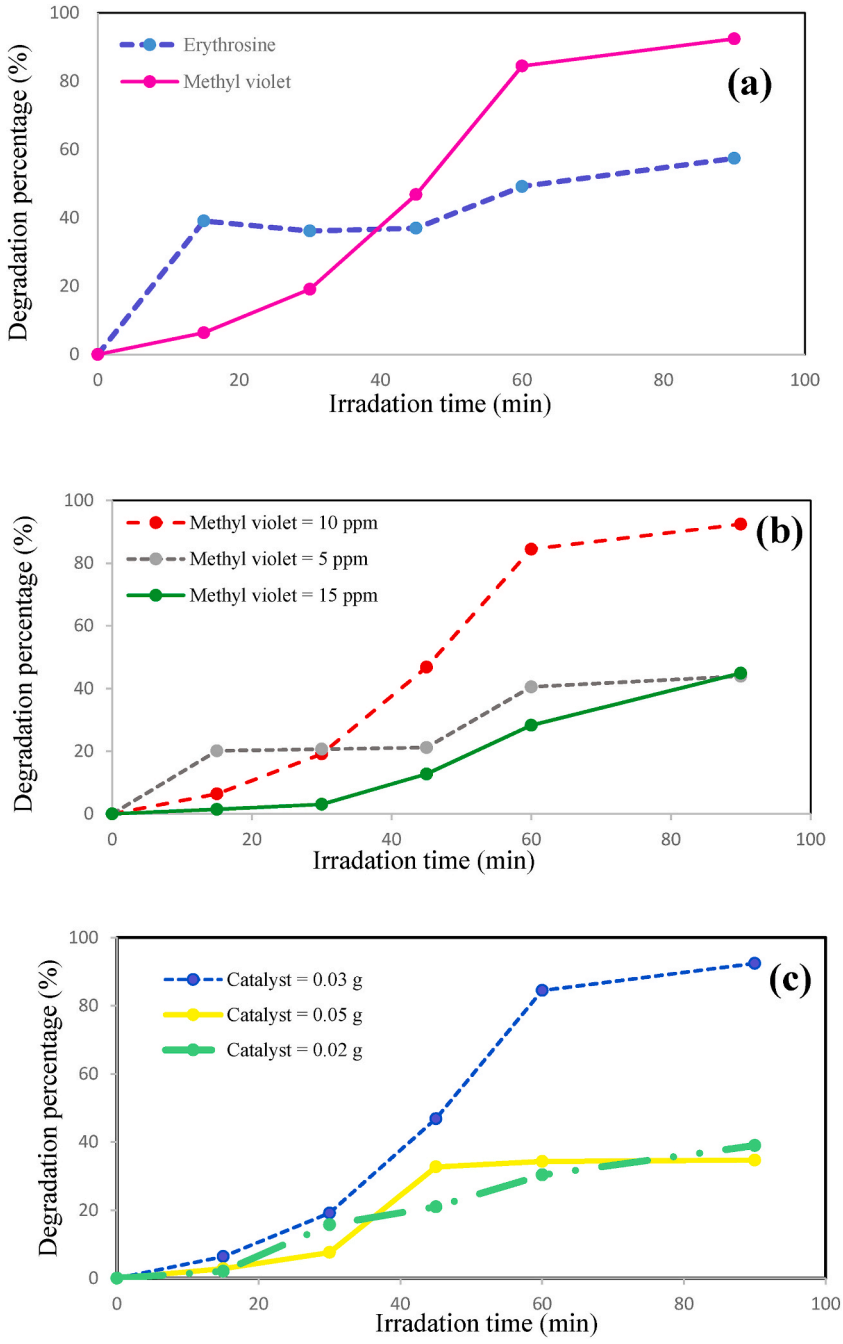

Fig. 9. The photocatalytic performance of sample 1 under visible light irradiation and investigation of the effects of: (a) dye type, (b) dye concentration and (c) photocatalyst dose.

are summarized in Fig. 10a. Without the ZMO photocatalyst, the degradation percentage of these dyes is low, as shown in Fig. 10a. This figure shows the importance of the ZMO photocatalysts in the degradation and removal of organic dyes. We repeated destruction reactions to determine the stability of the photocatalyst (sample 1). We repeated six consecutive reaction cycles for the photocatalyst toward the MV. We filtered, washed, and dried the photocatalyst after any cycles and observed a little activity loss after six consecutive reactions (Fig. 10b). We related this result to the high stability of the ZMO NSs synthesized in this work. The observed activity loss of the photocatalyst after any cycle is due to a decrease in the dye concentration because of its absorbance on the surface of the photocatalyst. Results obtained from repeated destruction reactions show the as-synthesized ZMO NSs have a high potential to utilize as a photocatalyst under visible light irradiation. We used two scavengers to investigate the degradation mechanism of MV by ZMO NSs and introduce the active species in MV degradation because the scavengers quench these species in the degradation process. The TBA and

Table 5
The results of the photocatalyst tests for the ZMO NSs.

Photocatalyst	Degradation%							Amount of photocatalyst (g)
	MV (10 ppm)	ES (10 ppm)	EBT (10 ppm)	EBT (5 ppm)	EBT (15 ppm)	MV (15 ppm)	MV (5 ppm)	
Sample 3	7.38	7.94	60.64	41.71	22.29	–	–	0.03
	–	–	37.96	–	–	–	–	0.02
	–	–	33.54	–	–	–	–	0.05
Sample 1	92.43	57.44	–	–	–	44.90	43.93	0.03
	34.66	–	–	–	–	–	–	0.05
	38.95	–	–	–	–	–	–	0.02

BQ were used as scavengers to detect the formation of hydroxyl and superoxide radicals, respectively. Fig. 10c shows the effect of the scavenger on the degradation of the MV solution. The photocatalytic degradation of MV (10 ppm) with ZMO NS (0.03 g) was 92.43 % after 90 min under visible light irradiation, as shown in Figs. 9 and 10. The photocatalytic degradation of MV decreased to 53.48 % and 60.63 % in the presence of TBA and BQ, respectively. This decrease indicates that OH° and $O_2^{\circ -}$ radicals are important active species in the MV degradation process. When a photocatalyst absorbs a photon, often the electron is excited into the conduction band and leaves a hole in the valence band. Then the water molecules are oxidized to H^+ and OH° by the holes in the valence band. The migrated electron reacts with dissolved O_2 in water to generate $O_2^{\circ -}$ radicals [51–55]. According to the results of the radical scavengers, we describe the below mechanism for MV degradation in this study:

$$\text{ZMO NS} \rightarrow \text{ZMO NS}\ (e^-_{CB} + h^+_{VB}) \quad (3)$$

$$\text{ZMO NS}\ (h^+_{VB}) + H_2O \rightarrow \text{ZMO NS} + H^+ + OH^{\circ} \quad (4)$$

$$\text{ZMO NS}\ (e^-_{CB}) + O_2 \rightarrow \text{ZMO NS} + O_2^{\circ -} \quad (5)$$

$$O_2^{\circ -} + H^+ \rightarrow HO_2^{\circ} \quad (6)$$

$$MV + OH^{\circ} \rightarrow \text{degradation} \quad (7)$$

$$MV + h^+_{VB} \rightarrow \text{oxidation} \quad (8)$$

$$MV + e^-_{CB} \rightarrow \text{reduction} \quad (9)$$

4. Conclusion

In this article, we describe two different synthesis methods, characterizations, properties, and applications of ZMO NSs. Two simple methods including hydrothermal and co-precipitation were selected. The magnetic, optical, and photocatalytic properties of the products were studied. ZMO NSs were used to remove three dyes (MV, ES, and EBT). The photocatalytic degradation was performed with three different photocatalyst doses and dye concentrations. The results demonstrated that the dye adsorption on the ZMO surfaces depends on photocatalyst dose and dye concentration. High degradation percent of MV (about 92 %) occurred with 0.03 g photocatalyst and 10 ppm MV solution. The recycle ability of ZMO NSs after six runs was checked. The efficiency reached from the first run to the fourth run from 92 % to 91 %. Thus, ZMO NSs have stable activity for MV degradation. It demonstrates that zinc manganite is a promising photocatalyst for organic dye degradation. We also investigated the mechanism of the degradation by using the scavengers. The obtained results proved that the degradation of MV occurred by the direct oxidization of OH° and $O_2^{\circ -}$ radicals.

Ethics declarations

All participants provided informed consent to participate in the study.

Data availability statement

No data was used for the research described in the article.

CRediT authorship contribution statement

Azam Sobhani: Writing – review & editing, Writing – original draft, Methodology. **Samira Alinavaz:** Investigation.

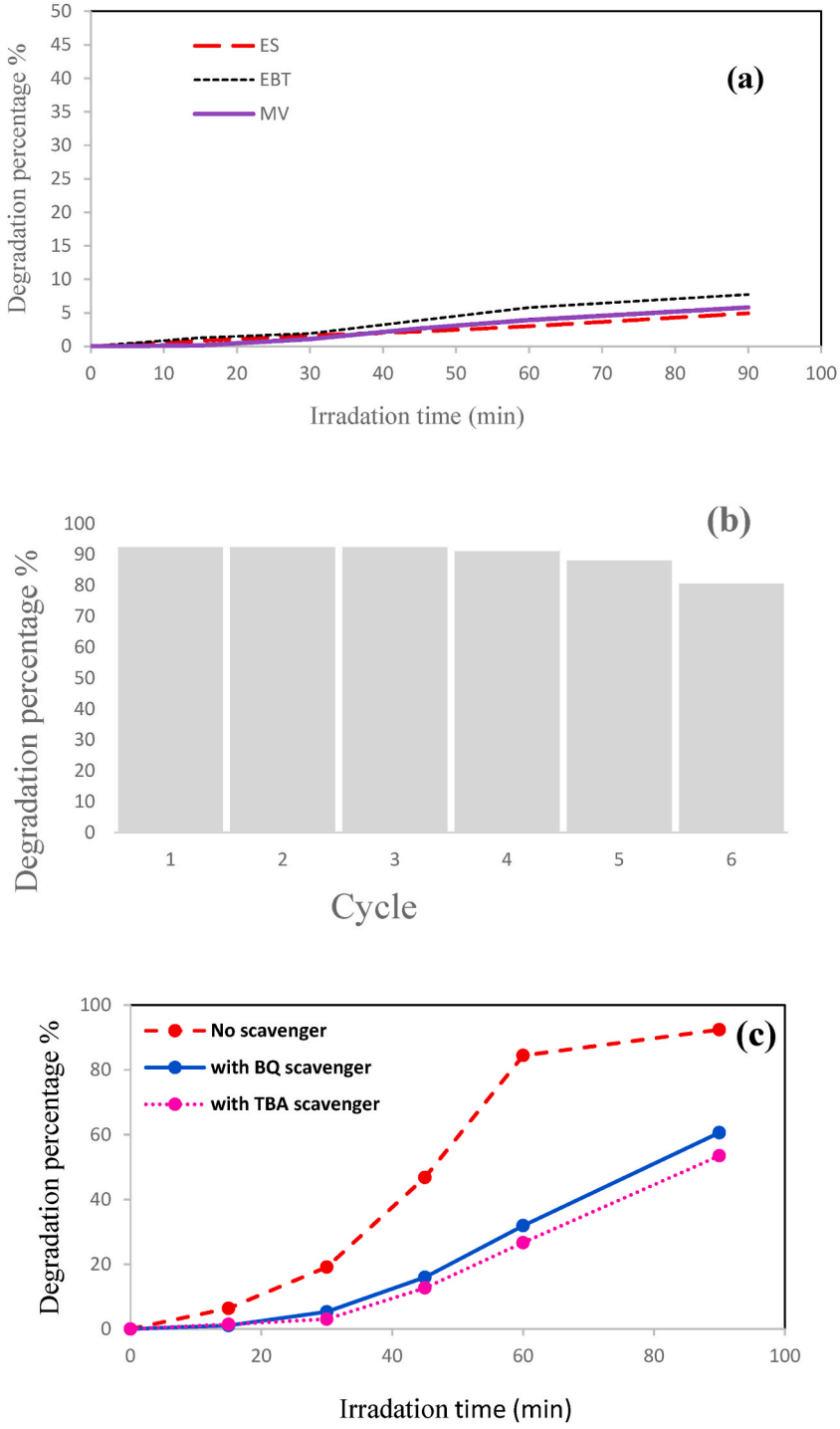

Fig. 10. (a) The degradation of MV, ES and EBT without ZMO photocatalyst, (b) Recycling tests of sample 1 for MV degradation under visible light irradiation, (c) effects of BQ and TBA scavengers on MV degradation in the presence of ZMO NSs under visible light Irradiation.

Declaration of competing interest

The authors declare that they have no known competing financial interests or personal relationships that could have appeared to influence the work reported in this paper.

Acknowledgment

This work is based upon research funded by Iran National Science Foundation (INSF) under project No. 4013370.

References

[1] L. Mamy, D. Patureau, E. Barriuso, C. Bedos, F. Bessac, X. Louchart, F. Martinlaurent, C. Miege, P. Benoit, Prediction of the fate of organic compounds in the environment from their molecular properties, Crit. Rev. Environ. Sci. Technol. 45 (2015) 1277–1377.
[2] R.B. Narayan, R. Goutham, B. Srikanth, K.P. Gopinath, A novel nano-sized calcium hydroxide catalyst prepared from clam shells for the photodegradation of methyl red dye, J. Environ. Chem. Eng. 6 (2018) 3640–3647.
[3] M.F. Hanafi, N. Sapawe, A review on the water problem associate with organic pollutants derived from phenol, methyl orange, and remazol brilliant blue dyes, Mater. Today: Proc. 31 (2020) A141–A150.
[4] S. Kumar, S.K. Sharma, R.D. Kaushik, L.P. Purohit, Chalcogen-doped zinc oxide nanoparticles for photocatalytic degradation of Rhodamine B under the irradiation of ultraviolet light, Mater. Today Chem. 20 (2021), 100464.
[5] M. Mahdiani, A. Sobhani, M. Salavati-Niasari, The first synthesis of $CdFe_{12}O_{19}$ nanostructures and nanocomposites and considering of magnetic, optical, electrochemical and photocatalytic properties, J. Hazard Mater. 367 (2019) 607–619.
[6] R. Mohassel, A. Sobhani, M. Salavati-Niasari, M. Goudarzi, Pechini synthesis and characteristics of Gd_2CoMnO_6 nanostructures and its structural, optical and photocatalytic properties, Spectrochim. Acta, Part A 204 (2018) 232–240.
[7] S. Bayat, A. Sobhani, M. Salavati-Niasari, Co_2SiO_4 nanostructures/nanocomposites: synthesis and investigations of optical, magnetic, photocatalytic, thermal stability and flame retardant properties, J. Mater. Sci. Mater. Electron. 29 (2018) 7077–7089.
[8] Z. Asgari Fard, A. Sobhani, R. Monsef, M. Salavati-Niasari, Lead carbonate hydroxide nanostructures: a new hydrothermal synthesis in the presence of ethylenediamine and hydrazine and investigation photocatalytic behavior, J. Mater. Sci. Mater. Electron. 30 (2019) 20947–20957.
[9] Z. Zheng, Y. Cheng, X. Yan, R. Wang, P. Zhang, Enhanced electrochemical properties of graphene-wrapped $ZnMn_2O_4$ nanorods for lithium-ion batteries, J. Mater. Chem. 2 (2014) 149–154.
[10] M.Y. Nassar, M. Khatab, Cobalt ferrite nanoparticles via a template-free hydrothermal route as an efficient nano adsorbent for potential textile dye removal, RSC Adv. 6 (2016) 79688–79705.
[11] M.Y. Nassar, S. Abdallah, Facile controllable hydrothermal route for a porous $CoMn_2O_4$ nanostructure: synthesis, characterization, and textile dye removal from aqueous media, RSC Adv. 6 (2016) 84050–84067.
[12] N. Guo, X.Q. Wei, X.L. Deng, X.J. Xu, Synthesis and property of spinel porous $ZnMn_2O_4$ microspheres, Appl. Surf. Sci. 356 (2015) 1127–1134.
[13] W. Dang, F. Wang, Y. Ding, C. Feng, Z. Guo, Synthesis and electrochemical properties of $ZnMn_2O_4$ microspheres for lithium-ion battery application, J. Alloys Compd. 690 (2017) 72–79.
[14] M.Y. Nassar, T.Y. Mohamed, I.S. Ahmed, One-pot solvothermal synthesis of novel cobalt salicylaldimine–urea complexes: a new approach to Co_3O_4 nanoparticles, J. Mol. Struct. 1050 (2013) 81–87.
[15] M.Y. Nassar, Size-controlled synthesis of $CoCO_3$ and Co_3O_4 nanoparticles by free-surfactant hydrothermal method, Mater. Lett. 94 (2013) 112–115.
[16] M.Y. Nassar, I.S. Ahmed, Template-free hydrothermal derived cobalt oxide nanopowders: synthesis, characterization, and removal of organic dyes, Mater. Res. Bull. 47 (2012) 2638–2645.
[17] S. Kumar, R.D. Kaushik, L.P. Purohit, Hetro-nanostructured Se-ZnO sustained with RGO nanosheets for enhanced photocatalytic degradation of p-Chlorophenol, p-Nitrophenol and Methylene blue, Sep. Purif. Technol. 275 (2021), 119219.
[18] F.M. Courtel, H. Duncan, Y. Abu-Lebdeh, I.J. Davidson, High capacity anode materials for Li-ion batteries based on spinel metal oxides AMn_2O_4 (A = Co, Ni, and Zn), J. Mater. Chem. 21 (2011) 10206–10218.
[19] F.M. Courtel, Y. Abu-Lebdeh, I.J. Davidson, $ZnMn_2O_4$ nanoparticles synthesized by a hydrothermal method as an anode material for Li-ion batteries, Electrochim. Acta 71 (2012) 123–127.
[20] X. Luo, X. Zhang, L. Chen, L. Li, G. Zhu, G. Chen, D. Yan, H. Xu, A. Yu, Mesoporous $ZnMn_2O_4$ microtubules derived from a biomorphic strategy for high-performance lithium/sodium ion batteries, ACS Appl. Mater. Interfaces 10 (2018) 33170–33178.
[21] R. Gherbi, Y. Bessekhouad, M. Trari, Structure, optical and transport properties of Mg-doped $ZnMn_2O_4$, J. Alloys Compd. 655 (2016) 188–197.
[22] G. Fierro, M. Lo Jacono, M. Inversi, R. Dragone, G. Ferraris, Preparation, characterization and catalytic activity of Co–Zn-based manganites obtained from carbonate precursors, Appl. Catal., B 30 (2001) 173–185.
[23] L. Zhao, X. Li, J. Zhao, Fabrication, characterization and photocatalytic activity of cubic-like ZnMn2O4, Appl. Surf. Sci. 268 (2013) 274–277.
[24] C. Chanel, S. Fritsch, C. Drouet, A. Rousset, M.L. Martınez Sarrion, L. Mestres, M. Morales, Synthesis, thermogravimetric and high temperature X-ray diffraction analyses of zinc-substituted nickel manganites, Mater. Res. Bull. 35 (2000) 431–439.
[25] R. Gherbi, Y. Bessekhouad, M. Trari, Optical and transport properties of Sn-doped $ZnMn_2O_4$ prepared by sol–gel method, J. Phys. Chem. Solid. 89 (2016) 69–77.
[26] G.D. Park, Y.C. Kang, J.S. Cho, Morphological and electrochemical properties of $ZnMn_2O_4$ nanopowders and their aggregated microspheres prepared by simple spray drying process, Nanomaterials 12 (2022) 680–690.
[27] S.V. Lakshmi, S. Pauline, Structural, morphological and optical properties of hetarolite-$ZnMn_2O_4$ nanoparticle by hydrothermal method, Int. J. Sci. Res. (2014) 14–18.
[28] X.D. Zhang, S.Z. Wu, J. Zang, D. Li, Z.D. Zhang, Hydrothermal synthesis and characterization of nano crystalline Zn-Mn spinel, J. Phys. Chem. Solid. 68 (2007) 1583–1590.
[29] P. Zhang, X. Li, Q. Zhao, S. Liu, Synthesis and optical property of one-dimensional spinel ZnMn2O4 nanorods, Nanoscale Res. Lett. 6 (2011) 323–330.
[30] M.Y. Nassar, E.A. El-Moety, M.F. El-Shahat, Synthesis and characterization of a $ZnMn_2O_4$ nanostructure as a chemical nanosensor: a facile and new approach for colorimetric determination of omeprazole and lansoprazole drugs, RSC Adv. 7 (2017) 43798–43811.
[31] S. Taghavi Fardood, F. Moradnia, A. Ramazani, Green synthesis and characterisation of $ZnMn_2O_4$ nanoparticles for photocatalytic degradation of Congo red dye and kinetic study, Micro & Nano Lett. 14 (2019) 986–991.
[32] J. Bhagwan, N. Kumar, K.L. Yadav, Y. Sharma, Probing the electrical properties and energy storage performance of electrospun $ZnMn_2O_4$ nanofibers, Solid State Ionics 321 (2018) 75–82.
[33] B. Fan, A. Hu, X. Chen, S. Zhang, Q. Tang, J. Wang, W. Deng, Z. Liu, K. Xiao, Hierarchical porous $ZnMn_2O_4$ microspheres as a high-performance anode for lithium-ion batteries, Electrochim. Acta 213 (2016) 37–45.
[34] J. Zhao, F. Wang, P. Su, M. Li, J. Chen, Q. Yang, C. Li, Spinel ZnMn2O4 nanoplate assemblies fabricated via "escape-by-crafty-scheme" strategy, J. Mater. Chem. 22 (2012) 13328–13333.
[35] Y. Zhang, Y. Zhang, C. Guo, B. Tang, X. Wang, Z. Bai, Porous ZnMn2O4 nanowires as an advanced anode material for lithium ion battery, Electrochim. Acta 182 (2015) 1140–1144.

[36] Y. Zhang, P. Zhang, Y. Xu, X. Song, H. Wang, T. Ma, Synthesis of pomegranate-shaped micron ZnMn2O4 with enhanced lithium storage capability, J. Materiomics 7 (2021) 699–707.
[37] A. Sobhani, M. Salavati-Niasari, Optimized synthesis of ZnSe nanocrystals by hydrothermal method, J. Mater. Sci. Mater. Electron. 27 (2016) 293–303.
[38] Z. Shahri, A. Sobhani, M. Salavati-Niasari, Controllable synthesis and characterization of cadmium molybdate octahedral nanocrystals by coprecipitation method, Mater. Res. Bull. 48 (2013) 3901–3909.
[39] Z. Azmoodeh, H. Milani Moghaddam, S. Nasirian, Hydrogen gas sensing feature of polypyrrole nanofibers assisted by spinel ZnMn2O4 microspheres in dynamic conditions, Int. J. Hydrogen Energy 47 (2022) 29971–29984.
[40] M. Annalakshmi, S. Kumaravel, T.S.T. Balamurugan, S.-M. Chen, J.-L. He, Facile solvothermal synthesis of ultrathin spinel $ZnMn_2O_4$ nanospheres: an efficient electrocatalyst for in vivo and in vitro real time monitoring of H_2O_2, J. Electroanal. Chem. 900 (2021), 115674.
[41] F. Zhu, J. Chen, J. Ma, S. Komarneni, Degradation of organic pollutants by $ZnMn_2O_4$/organic acid system: identification of active species, Mater. Lett. 293 (2021), 129725.
[42] N.M. Deraz, A.A. Abdeltawab, M.M. Selim, O. El-Shafey, A.A. El-Asmy, S.S. Al-Deyab, Precipitation–deposition assisted fabrication and characterization of nano-sized zinc manganite, J. Ind. Eng. Chem. 20 (2014) 2901–2904.
[43] F. uz Zaman, S. Nagamuthu, K. Cui, L. Hou, C. Yuan, Microwave-assisted synthesis of porous heterojunction $ZnO/ZnMn_2O_4$ microrods for efficient degradation of organic pollutants, Inorg. Chem. Commun. 144 (2022), 109845.
[44] G. Harini, A. Syed, M.K. Rahiman, A.H. Bahkali, A.M. Elgorban, R.S. Varma, S. Sudheer Khan, Enhanced photodegradation of rifampicin and co-trimoxazole by $ZnO/ZnMn_2O_4$/ZnS-PVA and its genotoxicity studies on Allium cepa, Chemosphere 308 (2022), 136238.
[45] J. Zia, E.S. Aazam, U. Riaz, Facile synthesis of MnO_2 nanorods and $ZnMn_2O_4$ nanohexagons: a comparison of microwave-assisted catalytic activity against 4-nitrophenol degradation, J. Mater. Res. Technol. 9 (2020) 9709–9719.
[46] R. Gherbi, M. Benamira, Y. Bessekhouad, Enhanced photoelectrochemical and photocatalytic properties of Mg doped $ZnMn_2O_4$, J. Alloys Compd. 851 (2021), 156797.
[47] Y. Bessekhouad, D. Robert, J.-V. Weber, Photocatalytic activity of Cu_2O/TiO_2, Bi_2O_3/TiO_2 and $ZnMn_2O_4/TiO_2$ heterojunctions, Catal. Today 101 (2005) 315–321.
[48] A. Sobhani, Hydrothermal synthesis of $CuMn_2O_4$/CuO nanocomposite without capping agent and study its photocatalytic activity for elimination of dye pollution, Int. J. Hydrogen Energy 47 (2022) 20138–20152.
[49] I. Janhavi, S.K. Singh, Photocatalytic detoxification method for zero effluent discharge in dairy industry: effect of operational parameters, Int. J. Chem. Biomol. Eng. 1 (2008) 160–164.
[50] F.A. Aisien, N.A. Amenaghawon, E.F. Ekpenisi, Photocatalytic decolourisation of industrial wastewater from a soft drink company, J. Eng. Appl. Sci. 9 (2013) 11–16.
[51] V. Gupta, S. Singh, Corona-poling enhanced photocatalytic degradation of methyl-violet and rhodamine B pollutants using ferroelectric nanoparticles, Chem. Inorg. Mater. 1 (2023), 100008.
[52] S. Kumar, R.D. Kaushik, G.K. Upadhyay, L.P. Purohit, rGO-ZnO nanocomposites as efficient photocatalyst for degradation of 4-BP and DEP using high temperature refluxing method in in-situ condition, J. Hazard Mater. 406 (2021), 124300.
[53] S. Kumar, R.D. Kaushik, L.P. Purohit, Novel ZnO tetrapod-reduced graphene oxide nanocomposites for enhanced photocatalytic degradation of phenolic compounds and MB dye, J. Mol. Liq. 327 (2021), 114814.
[54] S. Kumar, R.D. Kaushik, L.P. Purohit, RGO supported ZnO/SnO_2 Z-scheme heterojunctions with enriched ROS production towards enhanced photocatalytic mineralization of phenolic compounds and antibiotics at low temperature, J. Colloid Interface Sci. 632 (2023) 196–215.
[55] S. Kumar, R.D. Kaushik, L.P. Purohit, ZnO-CdO nanocomposites incorporated with graphene oxide nanosheets for efficient photocatalytic degradation of bisphenol A, thymol blue and ciprofloxacin, J. Hazard Mater. 424 (2022), 127332.